Materials Science-Poland, 40(1), 2022, pp. 25-48
http://www.materialsscience.pwr.wroc.pl/
DOI: 10.2478/msp-2022-0007

Weld defects and precipitates of deposited metal in 9Ni steel welded joint

Chengyong Ma[1], Yanchang Qi[1], Yuqing Zhang[1], Zhiquan Wu[2], Xin Zhang[2,*]

[1]Welding Research Institute, General Iron and Steel Research Institute, Beijing 100044, China
[2]Institute of New Energy Technology, State Power Investment Corporation Research Institute, Beijing 102209, China

Three kinds of electrode with different niobium contents were developed and compared, and the influence of alloying elements on microstructure and mechanical properties was summarized. Strong carbide elements such as Nb, Ti, and V were added to form stable precipitates. The existence of intercrystalline precipitates leads to pinning and zigzag of grain boundaries, hinders the propagation of cracks, and enhances the low temperature strength and impact toughness of the materials. The No. 1 and No. 2 ENiCrMo-6 electrodes meet the requirements of LNG (liquified natural gas) equipment. The tensile strength of the deposited metal reaches 687 MPa, while the average impact energy at −196°C is 131 J. Owing to fluctuations in the stress concentration at the junction of grain boundaries, cracks may easily form. MC carbide can retard the crack propagation. With the increase of Nb and other alloys, the strength and hardness increase gradually, but the plasticity and toughness are retarded to a certain extent.

Keywords: *deposited metal, 9Ni steel, welded joint, precipitate*

1. Introduction

9Ni steel is a kind of martensite-bainite, low carbon, quenched and tempered steel with good toughness and high strength at very low temperature [1]. Compared with austenitic stainless steel, 9Ni steel has the advantages of small thermal expansion coefficient, high strength, low temperature toughness, excellent welding performance, and good economy [2, 3]. It has become one of the main materials for manufacturing large LNG storage tanks.

A great deal of work has been done on 9Ni steel. The existing reports focus on the study of low temperature and fracture properties [4, 5]. In actual production practice, arc welding is the predominant method employed for welding 9Ni steel, followed by submerged arc welding and tungsten inert gas arc welding, while SMAW (shielded metal arc welding) is the most efficient and commonly used welding methods in the fabrication of 9Ni steel storage tanks. Aiming at the construction of a 20,000 m^3 LNG cryogenic storage tank, Wu and Jiang [6] realized the welding of 9Ni steel by submerged arc automatic transverse welding.

9Ni steel needs to work at ultra-low temperature; so, its welded joint must have good low temperature toughness. There is thus a need to avoid overheating and grain growth in the welding of structures made of 9Ni steel. Therefore, the welding of 9Ni steel must be accompanied with the following measures [7, 8]: no preheating before welding and strict control over the interlaminar temperature; choosing the appropriate line energy; using multilayer multipass welding and avoiding single pass welding; and selection of AC polarity current, hot crack control, cold crack control, and other measures. Changhua [9] has completed the determination and analysis of an SH-CCT diagram of 22.1 mm steel with 9%Ni wall thickness to provide technical support for the rational formulation of welding process; discovered the influence law of welding current, drying temperature, and holding time on diffusion hydrogen of deposited metal; and put forward a reasonable drying system for reducing hydrogen content of welding electrode. The influence of temperature, ambient humidity, and

* E-mail: kmzx201@163.com

© Ma et al. 2021. This is an open access article distributed under the Creative Commons Attribution-NonCommercial-NoDerivatives 4.0 License. (http://creativecommons.org/licenses/by-nc-nd/4.0/)

preheating temperature on the cracks and surface cracks of Y-groove specimens was studied. The reasonable preheating temperature for preventing cold cracks in the welding of 9%Ni steel was proposed. In comparing the GTA welded joints with the laser beam welded joints, El-Batahgy et al. [10] found that higher tensile strength, fine martensitic microstructure, and impact fracture toughness values with much a lower mismatch were obtained for laser beam welded joints. The lower-mismatch impact fracture toughness obtained (1.37 J/mm^2) was much higher than that of the GTA welded joints (0.78 J/mm^2). A better combination of tensile strength and impact toughness of the concerned steel welded joints is assured by autogenous laser beam welding process. Mu et al. [11] studied the fracture toughness of 9%Ni steel by conducting the crack tip opening displacement (CTOD) test at various temperatures. Their investigations revealed that with the increase of welding heat input, the austenitic fraction of the weld increased but the number of precipitated phases decreased. The fatigue crack propagated modes and the influences of the precipitates were determined under various temperatures.

At present, ENiCrMo-6 and ENiCrMo-3 are the two most widely used nickel-based electrodes for welding 9Ni steel both domestically and abroad, but the electrodes ENiCrFe-4, ENiCrFe-9, ENiMo-8, and ENiMo-9 have also been applied to some extent. Li and Yang [12] suggested measures to control the formation of hot cracks in welded 9Ni steel, and developed submerged arc welding flux CHF205 and matching wire CHW-NiCrMo-3 as well as flux CHF206 and matching wire CHW-NiCrMo-4; these can easily remove slag from weld seam without slag inclusion, undercut, and porosity, and the resultant weld has excellent plasticity, toughness, and crack resistance.

At present, 9Ni steel is widely used as the material for the fabrication of LNG storage tank, but there are still many problems in welding. For instance, welding needs to be carried out in conjunction with other welding materials, there are no special matching welding materials available, and so on. To further improve the weldability of 9Ni steel, there is an imminent need to develop a high-strength and tough welding material. According to the strengthening theory, niobium and other alloying elements have great influence on the formation and mechanical properties of intermetallic compounds. Therefore, three kinds of electrode with different niobium contents were developed and compared, and the influence of alloying elements on microstructure and mechanical properties was summarized in order to provide an experimental basis for the development of nickel-based alloy electrode for LNG.

2. Experimental materials and experimental methods

2.1. Test material

2.1.1. Test steel plate

The 9Ni steel used as an experimental material in this study was procured from Anshan Iron and Steel Group. The test 9Ni steel is a quenched and tempered state. The length of the test 9Ni steel is measured along the direction of rolling, the thickness of the plate is 20 mm, and the chemical composition of the steel is shown in Table 1.

Table 1. Chemical composition of 9Ni steel/wt.%

C	Si	Mn	S	P	Ni	Fe
0.05	0.45	0.62	0.001	0.0024	9.35	Balance

2.1.2. Composition design of electrode

The 9Ni steel used for LNG storage tank has the characteristics of low temperature, high strength, and high toughness.

It is required that the weld metal matched with 9Ni steel also have high strength and toughness reserves, and the main difficulty involved in the manufacture of 9Ni steel electrode is to maintain the strength of weld metal while also maintaining its plasticity and toughness at a high level.

According to the theory of alloying and the mechanism of strengthening and toughening, the composition and content of the drug skin are rationally distributed. The chemical components of the three kinds of welding rods matched by the developed 9Ni steel are shown in Table 2. The diameter

Table 2. Chemical composition of the weld metal (wt%)

No.	C	Si	Mn	Nb	W	Cr	Mo	P/S	Ti	Ni
1#	0.03–0.05	0.2–0.4	3.2–3.8	1.10	1.6–1.8	12.5–13.0	7.4–7.7	≤ 0.015	0.10–0.13	Bal.
2#	0.03–0.05	0.2–0.4	3.2–3.8	1.30	1.6–1.8	12.5–13.0	7.4–7.7	≤ 0.015	0.10–0.13	Bal.
3#	0.03–0.05	0.2–0.4	3.2–3.8	1.52	1.6–1.8	12.5–13.0	7.4–7.7	≤ 0.015	0.10–0.13	Bal.

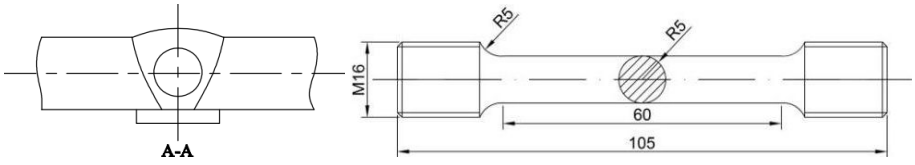

Fig. 1. Tensile specimen of deposited metal and its sampling position

of the flux core of the electrode is 4 mm, and the outer diameter of the electrode is 6.5 mm.

2.2. Test method

2.2.1. Metal coloring flaw detection

After the welding of the deposited metal, the specimen is tested once the fine grinding is complete. Once the processes of fine grinding and drying have been carried out on the sample, spray permeation agent is used in the spray irrigation. After the penetration, the surface is wiped, and then the imaging agent is shaken well and sprayed on the surface of the sample. Once a suitable quantum of time has been allowed to elapse for the imaging, the defect on the surface of the specimen is observed. Three parallel samples are used for each test, and the final value is the average of the three samples.

2.2.2. Mechanical properties test of deposited metal

The sampling position and size of the tensile specimen of the deposited metal are shown in Figure 1. The test equipment is WE-300 hydraulic universal testing machine supplied by Shandong WanChen Testing Machine Co., Ltd.. The test temperature is room temperature.

2.2.3. Chemical composition and microstructure of deposited metal

ICP-AES supplied by NCS Testing Machine Co., Ltd. was used to analyze the chemical composition of the test. A 10% chromic acid corroding agent was used for electrolytic corrosion. The corrosion process was attended with constant voltage and constant current corrosion; the voltage was maintained at 3 V while the current at 1 A. The metallographic specimen and metallographic surface both needed to be immersed in the corrosion process. After corroding for 1 min, the surface was wiped with oxalic acid immediately to ensure the absence of residual corrosion. The sample was cleaned repeatedly in distilled water and then dried with a blower.

2.2.4. Analysis of precipitates and micromorphology of deposited metal

The distribution of precipitates was observed and collected using an OLYMPUS GX51 supplied by Olympus Corporation inverted metallographic microscope. The SISC IAS8.0 metallographic analysis software supplied by Beijing Zhongke Keyi Computer Technology Co., Ltd was used to analyze the size and size characteristics of the precipitates. Metallographic observation and collection were carried out using a Leica MEF-4M optical microscope supplied Coporation, which was also used to carry out the line measurement of columnar crystal (grain size). A HITACHI S-4300 type scanning electron microscopy (SEM, supplied HITACHI Coporation) equipped with an energy dispersive spectrometer (EDS) was used to carry out the morphology and energy spectrum analyses of the precipitation, microstructure, and inclusion.

Table 3. Welding parameters of deposited metal

Welding current (I/A)	Welding voltage (U/V)	Welding speed (v/cm/min)	Inter channel temperature (T/°C)	Heat input (E/kJ/cm)
95	27	13	100	a

2.2.5. Analysis of impact fracture of deposited metal

For the impact test of deposited metal, the V notch 55 mm × 10 mm × 10 mm standard sample is used. The notched position diagram is shown in Figure 2. The locations 1, 2, and 3 are weld center, fusion zone, and heat affected zone, respectively. The test equipment is JBZ-300B type automatic impact test machine supplied byvShandong WanChen Testing Machine Co., Ltd , the test temperature is −196°C, and the cooling medium is liquid nitrogen and anhydrous ethanol. After reaching the required temperature, it is still necessary to maintain the same temperature in the cooling box for 5 min and then carry out the test.

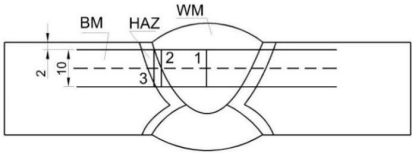

Fig. 2. Drawing of weld metal impact sampling

2.2.6. Hardness analysis of deposited metal

The test equipment used for assessing the hardness of the welding joint is HV-5 digital display Vivtorinox microscope supplied China Jinan Chenda Testing Machine Manufacturing Co., Ltd . Multilayer and multipass welding is used in welding, and the changes in the hardness of the weld and the heat affected zone cannot be guaranteed to be completely symmetrical. Therefore, the hardness test point is situated 2 mm beneath the surface of the weld, and the hardness test runs from one end of the welded joint, through the weld, and to the other end. The test point intervals of the weld of the parent material are 1 mm, 0.5 mm, and 2 mm, respectively. The position of hardness is shown in Figure 3.

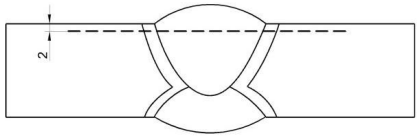

Fig. 3. Position diagram of welding joint hardness test position

2.2.7. Welding test of deposited metal

The test plate for metal welding is a quenched and tempered 9Ni steel plate with a size of 450 mm × 150 mm × 20 mm. The cushion plate is an 8 mm-thick tempered 9Ni steel plate. The size of the cladding metal slope is shown in Figure 4. A Miller Dimension 1250 welding machine supplied by Miller Coporation is used as the welding equipment, and electrode arc welding is adopted. In order to reduce the phenomenon of magnetic bias blowing, alternating current is used to carry out the welding. The process parameters are shown in Table 3.

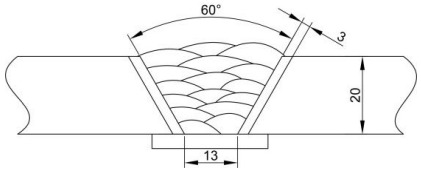

Fig. 4. Schematic diagram of welding groove

3. Results and analysis

3.1. Performance testing and penetration test of 9Ni steel

The mechanical properties of 9Ni steel are shown in Table 4. It can be seen that the mechanical properties of 9Ni steel are in conformity with the standard requirements. The microstructure and electron microscopic structure of 9Ni steel

Table 4. Mechanical properties of 9Ni steel

Tensile Strength (Rm/MPa)	**Yield strength ($Rp_{0.2}$/MPa)**	**Elongation (A/%)**	**Impact absorbing energy Akv/J (−196°C)**
727	668	27	231, 240, 233 234.7

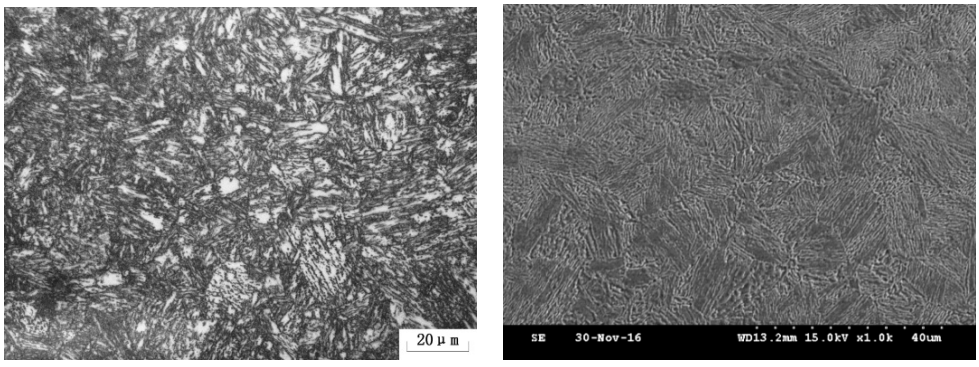

(A) (B)

Fig. 5. Microstructure and electron microscopic structure of 9Ni steel as observed by optical microscope **(A)** and SEM **(B)**. SEM, scanning electron microscopy

are shown in Figure 5. It can be seen that the microstructure of 9Ni steel is low carbon martensite.

The macro diagram of the deposited metal weld of 9Ni steel is shown in Figure 6. The deposited metal weld passes through the cross section of the weld through coloring penetration tests, as shown in Figure 7. It was found that 1# and 2# showed a perfect surface, and that the cross section of 3# deposited metal appeared in a red spot, which indicated that the cross section had defects.

Fig. 6. Macro diagram of metal weld bead

After cleaning the white imaging agent, a metallographic microscope is used to observe the defects. Pores are found at a defect, and their morphology is shown in Figure 8. The shape of the stomata is elliptical. It is believed that the solubility of oxygen, hydrogen, and carbon dioxide in the liquid nickel base alloy is large, but the solubility of these gases is greatly reduced in the solid state. So, the solubility of these gases in the deposited metal decreases when the molten metal is cooled from the high temperature liquid to the solid. The free gas cannot completely escape from the weld metal in the poor fluidity nickel base molten pool, which leads to the formation of pores.

The melting point of Ni is 1,446°C, while the melting point of nickel oxide (NiO) is 2,090°C, and the difference between these is large. Because of its small density, the oxide floats over the weld pool during the welding process. After the solidification, some of the oxide slag between the channels is not completely cleared. The high melting point oxide very easily forms slag between the channels, which can damage the strength and toughness of the weld metal. At present, the effective method is SMC, developed by Superalloy Company [13], who propose grinding or pickling as the main measures for cleaning the slag in time. Figure 9 is the SEM morphology of slag sandwiched between the welding channels.

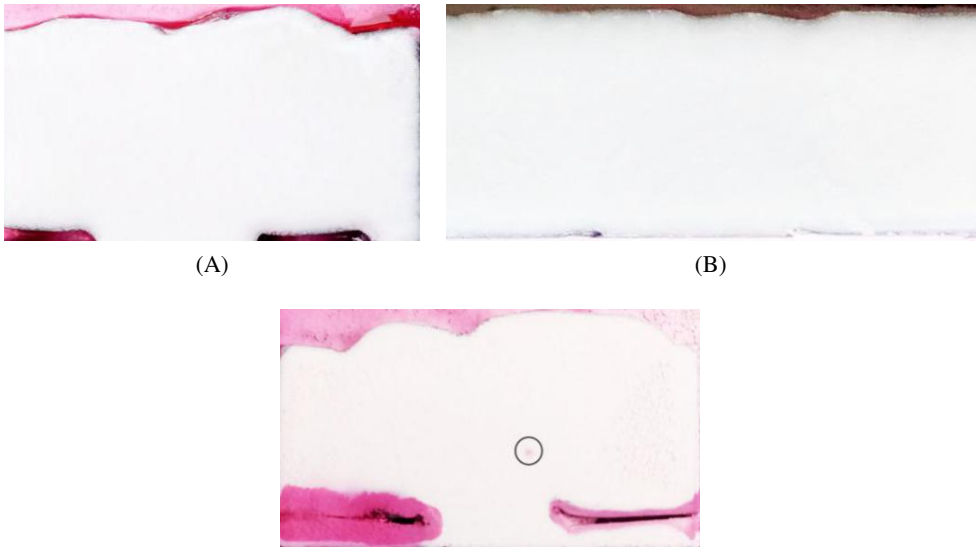

(A) (B)

(C)

Fig. 7. Penetration test of molten metal: **(A)** 1#; **(B)** 2#; **(C)** 3#

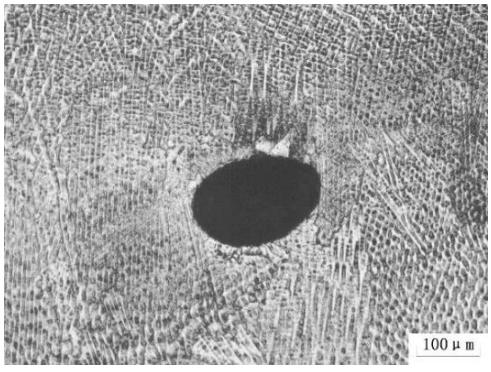

Fig. 8. Pore image under optical microscope

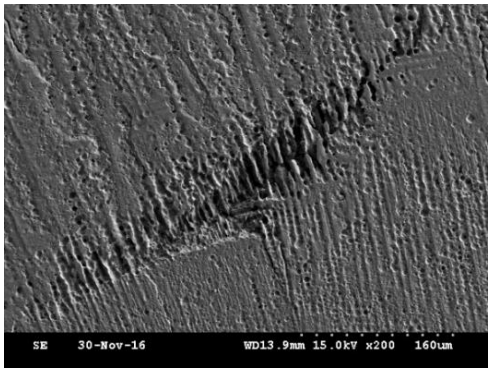

Fig. 9. Slag interlocking between welding channels

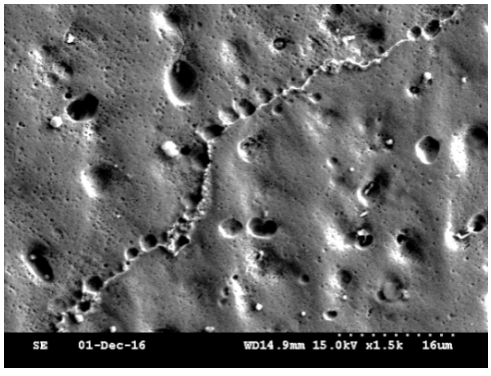

Fig. 10. Intergranular hole

Using SEM, it is further observed that there are pores in the 3# deposited metal along the grain boundary. These holes may be the reason for the formation of cracks under stress. The intergranular hole is shown in Figure 10.

Figures 11A and 11B show a crystal crack with a length of about 300 m. Figures 11C indicate the morphology and energy spectrum of the crack initiation site. It is found that the crack sprouts between the weld lines, and propagates along the dendritic boundaries; further, the main Ni and S elements exist at the cracking site. The composition of the precipitate in the 3# deposited metal is shown in Ta-

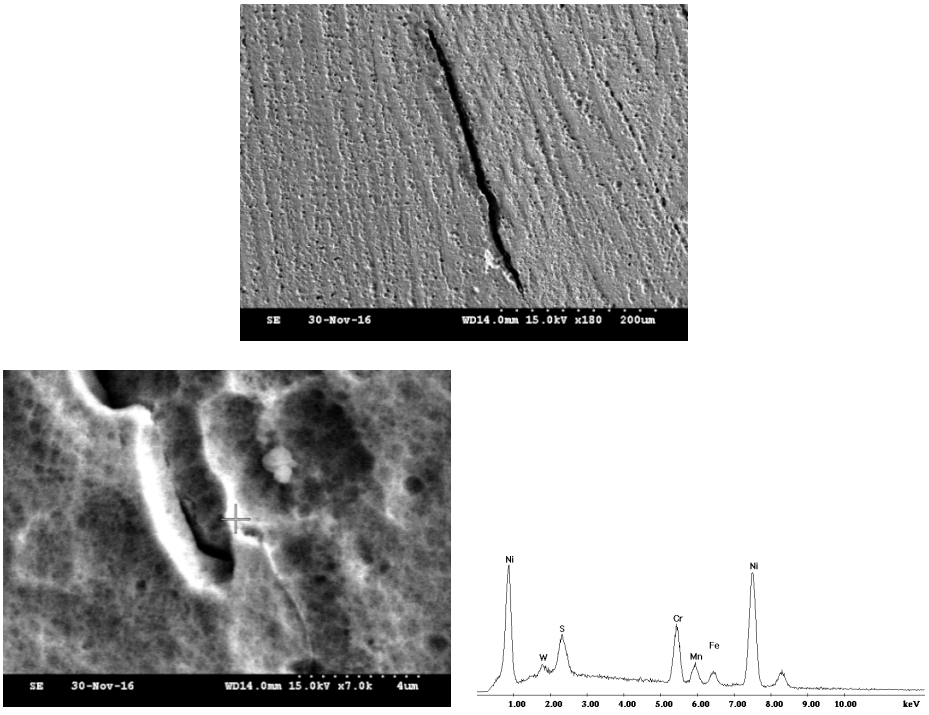

Fig. 11. Crack morphology and its energy spectrum of 3# deposited metal: **(A)** crystal crack; **(B)** morphology of crystal crack; **(C)** energy spectrum

ble 5. A study [14] found that at the late stage of solidification and crystallization, Ni3S2 eutectic with a melting point of 645°C is squeezed out and concentrated on the central position of columnar crystal to form a "liquid film", which continues to cool and contract and is subjected to tensile stress. In the process of tensile stress, the weak part becomes the source of the crack initiation, and eventually develops along the grain boundary to form the intergranular crack. On the other hand, the austenite gamma phase interface is easily wetted by the low melting point, and forms a continuous low melting point liquid film. The liquid film reduces the plasticity of the grain boundary, and it could very easily crack. The straight and smooth grain boundary provides a favorable condition for the crack growth. The cause of crack formation in 3# deposited metal is due to the fact that the high content of sulfur and Ni are segregated at the grain boundary to form low melting point eutectic, such as Ni3S2, which forms the "liquid film" at the end of the solidification of the weld metal. The tensile stress produced by the contraction causes the initiation of the crack.

Table 5. Precipitates' composition of 3# deposited metal (wt%)

Precipitates	**S**	**Cr**	**Mn**	**Fe**	**Ni**
Content	2.50	13.42	3.59	4.19	74.34

The solubility of S elements in the gamma matrix is very small, and there is a positive segregation during the solidification process. The impurity elements are harmful to the homogenization of the alloy components. Due to the continuous segregation of these impurities in the solidification front fluid during solidification, the solidification temperature of the remaining liquid decreases, resulting in the formation of low melting point compounds such as Ni3S2, which are the impurity elements in the final solidification zone of the alloy. The possibility of formation of Ni3S2 is analyzed based on the binary phase diagram and thermodynamic calculation [15]. The Van't Hof equation of free energy and the relationship between temperature and activity can be expressed as follows:

$$\Delta G = \Delta G^{\theta} + RT \ln J \tag{1}$$

where ΔG is the change of Gibbs free energy in the reaction process; ΔG^{θ} is the standard Gibbs free energy; R is the molar gas constant; T is the absolute temperature; and J is the activity ratio of reactants and products. In this experiment, the mole fraction was used instead of activity. As for the sulfide, the mole fraction of S at the opening crack is 2.70%, the melting point of Ni3S2 is 1,063 K, and the eutectic temperature of Ni-Ni3S2 is 918 K. The ΔG^{θ} value is calculated using the thermodynamic data. The known data are substituted in Eq. (1), and the calculated values are listed in Table 6. It can be seen from Table 5 that both the Ni3S2 at its melting temperature and the eutectic temperature formed by Ni-Ni3S2 are negative, which shows that the formation of this low melting point compound is completely possible in a nickel-based alloy. Obviously, the existence of these low melting point compounds and their eutectic is extremely harmful to the properties of the alloys, which is the main reason for the formation of intergranular cracks. We must strictly control the content of these harmful impurities.

Table 6. ΔG values at different temperatures

T/K	400	600	800	918	1,063
	−147.6	−142.2	−136.8	−125.4	−118.0

3.2. Microstructure and composition analysis of deposited metal

3.2.1. Microstructure

In multichannel and multichannel welding, the distribution and change of elements affect the quality of the welding to a great extent, and have a close relationship with the mechanical properties. Figure 12 is the macroscopic morphology of the cross section of the 2# deposited metal after corrosion. It is visible from Figure 12 that the deposited metal columnar crystal is developed, the weld columnar crystal near the fusion zone is perpendicular to the fusion line, and the grain grows along the fastest direction of heat dissipation. The columnar crystals between the various channels are mainly perpendicular to the interchannel interface, because its temperature gradient in this direction is larger. Figure 13 shows a columnar crystal of the root and surface of the 2# deposited metal. It is obvious that the columnar crystal structure of the welding root is more compact and the interdendritic distance is smaller. The SISC IAS8.0 metallographic analysis software was used to measure the dendrite width. The average dendrite width of the welding root is 12.56 μm, while the average surface width is 20.16 μm. This is due to the rapid cooling rate at the root of the weld. While the metal of the weld surface is affected by the heat of the front weld, the cooling rate and the grain growth speed slow down, and thus the columnar crystal structure is looser.

Fig. 12. Macromorphology of 2# deposited metal

Figure 14 shows the microstructure of three kinds of deposited metals. An IPP metallographic analysis software was used to measure the dendrite width of the deposited metal. The measured results show that the average dendrite widths and maximum widths of 1#, 2#, and 3# deposited metal are, respectively, 25.12 μm and 45.12 μm, 18.39 μm and 35.72 μm, and 13.18 μm and 19.27 μm. It is considered that the increase of alloying element content, especially the Nb element, plays a role in controlling the growth of dendrite through the pinning effect of precipitates, so that the dendrites of 3# deposited metal are denser than those of other deposited metals.

Figure 15 shows the austenite grain boundary microstructure of three kinds of deposited metals. The size of grain boundary was measured by an IPP analysis software. The measured results show that the average grain widths and maximum widths of 1#, 2#, and 3# deposited metals are, respectively, 84.29 μm and 132.87 μm, 71.67 μm and 124.91 μm, and 43.16 μm and 80.28 μm. It is believed that this is mainly due to the pinning effect of the precipitates containing Nb on the grain boundary, which hinders the growth of grain boundaries.

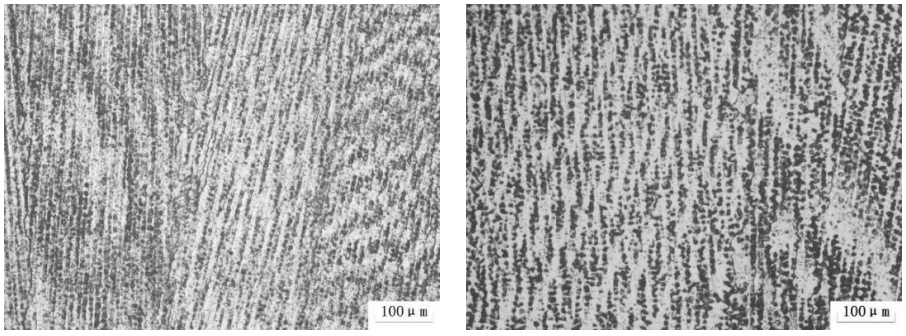

(A) (B)

Fig. 13. Microstructures of the root and surface of the deposited metal: **(A)** the root; **(B)** the surface

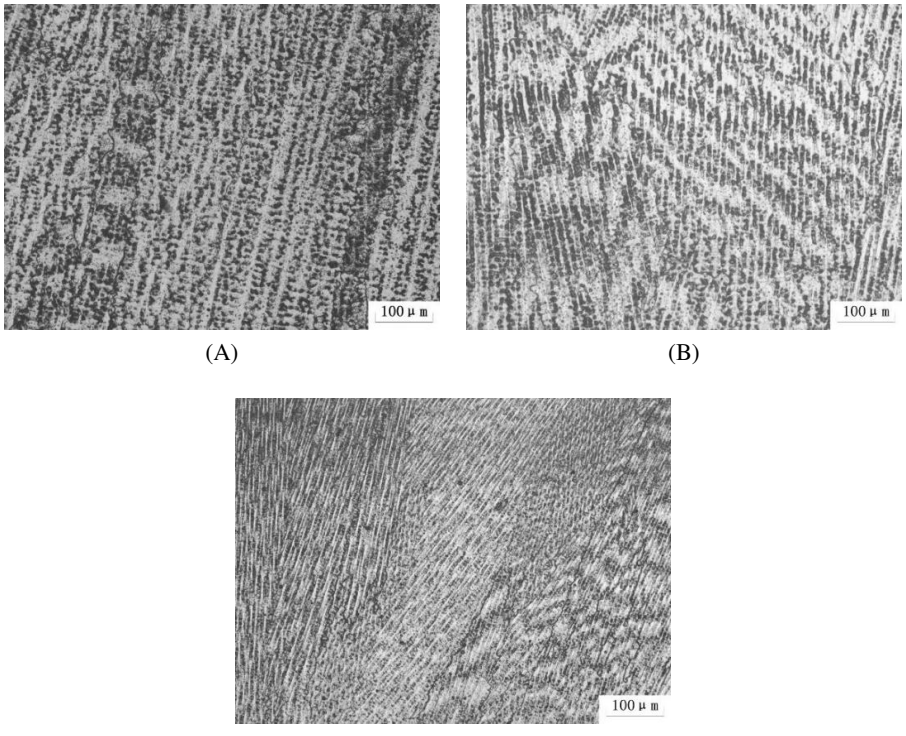

(A) (B)

(C)

Fig. 14. Microstructure of three kinds of deposited metals: **(A)** 1#; **(B)** 2#; **(C)** 3#

The more the Nb content, the greater the number of precipitates that occur. The more Nb elements are segregated on the grain boundaries, the more obvious the immobilization effect is on the grain boundaries, and thus the width of austenite grains gradually decreases.

Figure 16 shows the metallographic microstructure of the welding channels for the 2# deposited metal. In the case of multilayer and multipass welding, in order to study the change rule of element composition between welding channels, line scanning can be used to scan the welding channel on the deposited metals, and the changing trend of composition can be observed more clearly. The specific scanning position and the line scanning result of the element are shown in Figure 17. It can be

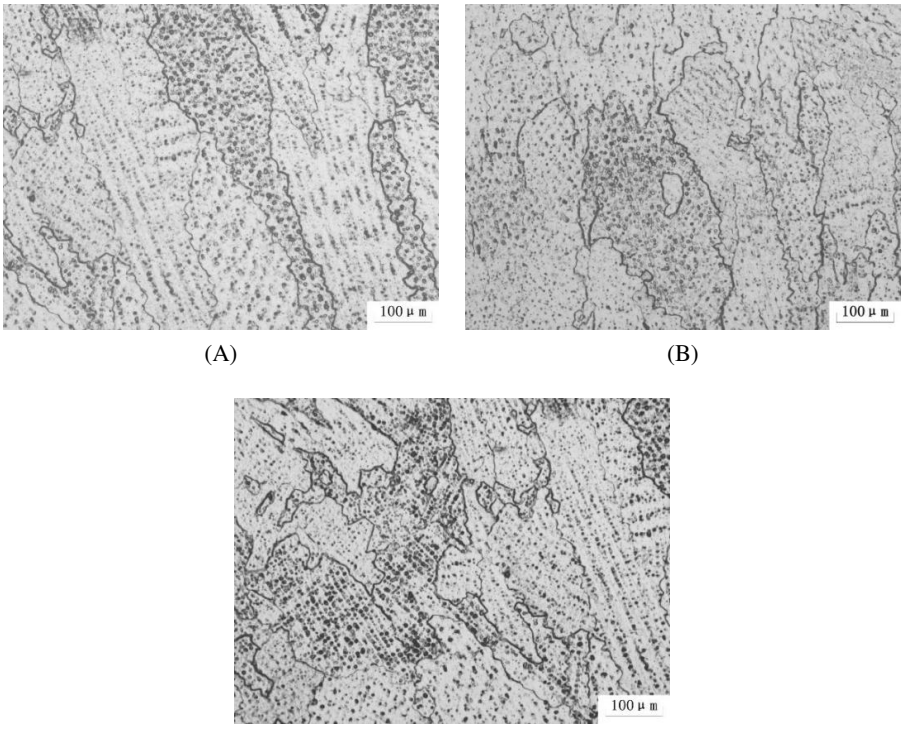

(A) (B)

(C)

Fig. 15. Austenite grain boundary microstructure of three kinds of deposited metals: **(A)** 1#; **(B)** 2#; **(C)** 3#

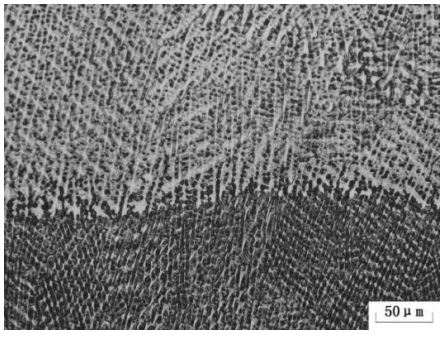

Fig. 16. Metallographic microstructure of the welding channels for the 2# deposited metal

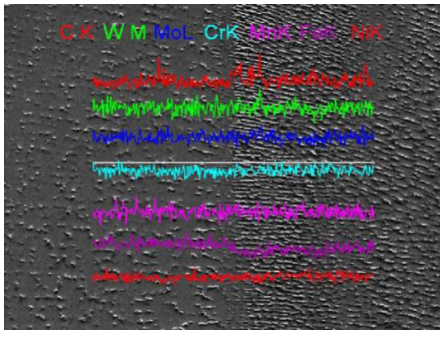

Fig. 17. Scanning position and the line scanning result of the element

seen from Figure 17 that the number of precipitated phases near the welding line is obviously increased compared with the previous welding line, which is due to the fast cooling rate at the interface of the weld and the segregation of elements in the solidification process. The results of component scanning showed that the content of C and Fe elements changed mainly in the composition of the weld. The content of Fe on the side of the rear welding channel is perceptibly reduced. The content of the C element is increased in the small part of the side of the rear welding channel, while the distribution of C elements at a distance far away from the interface of the welding channels is more stable. It is considered that this is related to the interdiffusion of elements in the solidification process of the weld pool between the welding channels [16]. The reason for the high content of Fe in the former

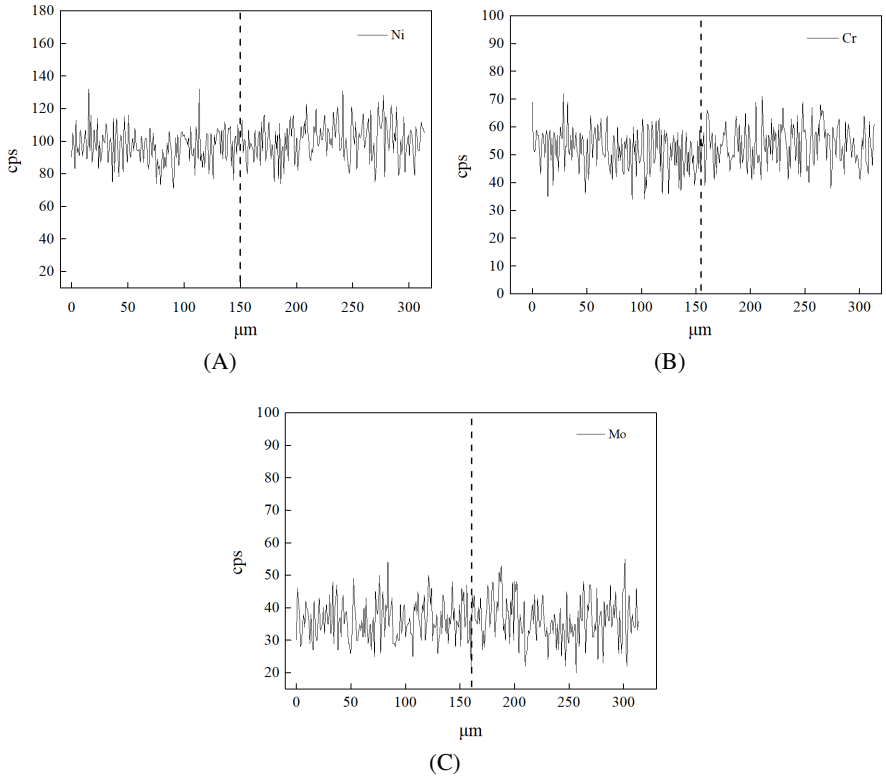

Fig. 18. Variations among Ni, Cr, and Mo contents within the 2# deposited metal weld: **(A)** Ni, **(B)** Cr, **(C)** Mo

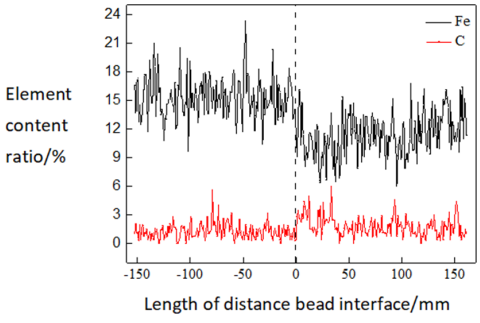

Fig. 19. Variation among Fe and C contents within the 2# deposited metal weld

welding channel is mainly due to the greater heating effect on the former welding channel during the subsequent welding of the next welding channel. The larger heating effect subjects the former weld to a partial remelting phenomenon. Due to the high melting point of Fe, the solidification of Fe between the welding channels is preferable during solidification. The lower melting point of the alloy elements in the next welding channel solidifies and forms the welding channel in the molten pool, which reduces the Fe content in the next welding channel. The diffusion coefficient of C is much larger than that of Ni, Cr, and other alloy elements, and has a strong trend of carbide precipitation. In addition, the solidification rate of interchannel interface is faster in the welding channel. Therefore, the segregation occurs near the interchannel interface to form carbide precipitation with high C content.

The distributions of main elements Ni, Cr, and Mo in the deposited metals were scanned and analyzed. The analysis results are shown in Figure 18. It can be seen that the contents of the three main elements of Ni, Cr, and Mo in the deposited metals are relatively stable in the weld channel, indicating that the content of these whole elements in the deposited metals are relatively homogeneous.

Figure 19 shows the change curves of Fe and C content at the weld interface. The left side is the first weld channel and the right side is the latter

weld channel. The content of Fe is about 10%–18%, and the total C content is about 2%. At the interface of the weld channels, the content of Fe decreases rapidly, and the Fe content of the right side adjacent to the interface of the weld channel is about 7%–11%. As the distance away from weld bead increases, the content of Fe increases. The content of C increases only at the interface of the weld channels, and the peak value reaches up to 6%. In the left side weld, the C content tends to be stable as a result of approaching the right side weld, and then decreases to 2%.

It can be speculated that the overall difference in the composition-mix of the elements of the welding metal is relatively small. The difference in the composition-mix of the elements comprising the welding metal existed only in relation to fluctuation of the content of two elements, Fe and C; and the amplitude of Fe element's fluctuation is relatively large. With the change of microstructure between the weld channels as observed under the metallographic microscope, the dendrite of the following channel is perceptibly larger than the previous one, and the content of the three main elements of Ni, Cr, and Mo have not changed perceptibly. Therefore, it is concluded that the change of the Fe element has an effect on the morphology of the γ austenite dendrite.

3.3. Precipitates and its strengthening and toughening effect in deposited metal

3.3.1. Intragranular precipitates

SEM electron microscope observation reveals that there are precipitates in the grain boundaries and grains in the three deposited metals, as shown in Figures 20 and 21. The precipitates are mainly precipitated phases of the Al and Ti oxides and the NbC and WC carbides. The main precipitate in the grains is NbC, which is divided into granular and long stripes. The diameter of the granular precipitate NbC is about 1 μm. The length and width of elongated precipitates' NbC are 2–3 μm and 1 μm, respectively. Through energy spectrum analysis, we ascertain that the granular precipitates mainly contain Nb, Al, and Ti, which are conjectured to be compound precipitates of carbides and oxides, and the main composition of long strip precipitates is NbC.

According to an analysis in the literature [17], the phases of the compound precipitates are formed by different stages of metallurgy and physicochemical reaction. According to the Ellingham oxygen potential diagram [18], as shown in Figure 22, the standard Gibbs free energy of the generation of Al_2O_3 and TiO_2 by Al, Ti, and O is very low, which means that the Al and Ti first combine with oxygen to form oxides after the pool reaction occurs. The oxide itself has higher melting point and preferentially precipitates from the matrix with lower dissolved oxygen capacity. In the process of rapid cooling and solidification of the molten pool, it becomes the center of carbide precipitation nucleation. In the nickel base alloy, the order of the stability of carbides formed by C and each element in turn is Ti > Nb > W > Mo > Cr > Mn > Fe, and finally the compound precipitates of carbides are formed with oxides. It is considered that these precipitates are embedded in the grain boundary and the matrix, have a strong effect on the strength of the crystal and the pinning of the grain boundary, and greatly affect the strength and toughness of the weld [19].

Besides, there are very few tungsten carbide precipitates in the crystal, and the morphology is shown in Figure 23. The width of the tungsten carbide is about 50 μm. The shape of the tungsten carbide is that of an elliptical white lump. Tungsten carbide is distributed around veins and reticular tissue. It is considered that under the action of the welding heat effect, the W in the electrode skin is dissolved in the molten pool. This is because in itself W is a strong negative segregation element; also, W easily combines with carbon to form WC with a high melting point. When the molten pool is cooled, the tungsten element first forms the precipitation of tungsten carbide in the crystal. The surrounding particles dissolve and the dissolved W elements react with Ni and Cr to form a eutectic structure with a low melting point. Owing to the fast cooling speed of the welding pool, the free-state eutectic microstructure is gathered around WC during cooling and solidification [21].

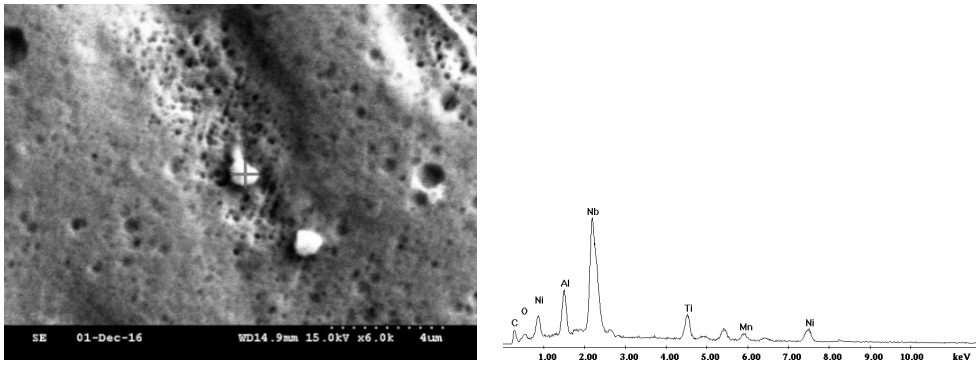

(A) (B)

Fig. 20. Precipitation and energy spectrum of granular Nb carbides

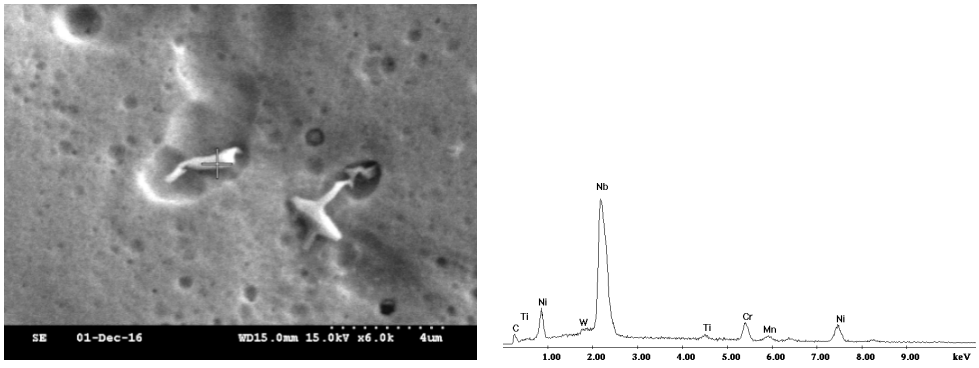

(A) (B)

Fig. 21. Precipitation and energy spectrum of long strip Nb carbides

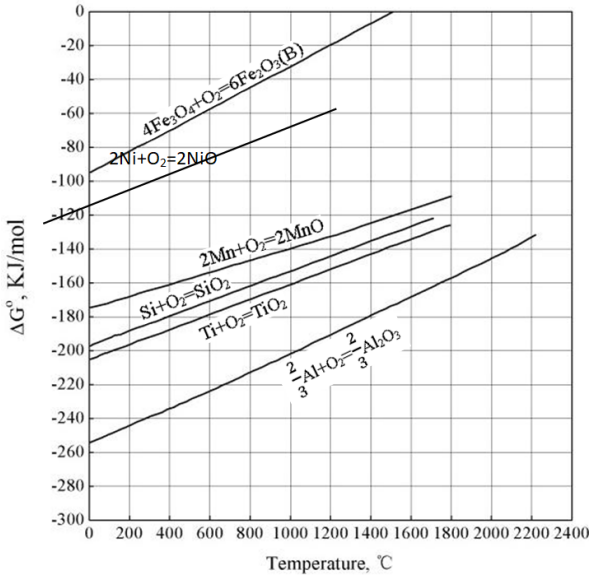

Fig. 22. Ellingham chart [20]

3.3.2. Precipitate on grain boundaries

The main precipitates at the grain boundary are shown in Figure 24. The composition of the main precipitates and that of the precipitates in the grain boundary are similar. The precipitates are mainly Al and Ti oxide precipitates. The main precipitates at grain boundaries are spherical and larger in size, but the number of main precipitates at grain boundaries is relatively small. This is due to the strong affinity between Al and oxygen, as a result of which alumina may form easily at grain boundaries. As the density of alumina is small and Al is a positive segregation element, the nucleation work of the nucleation at grain boundary is smaller; thus, oxide precipitation may easily form at the grain boundary.

The carbide of Nb precipitates at the grain boundary, as shown in Figure 25. The Nb carbides assume a strip shape. The width and length of the

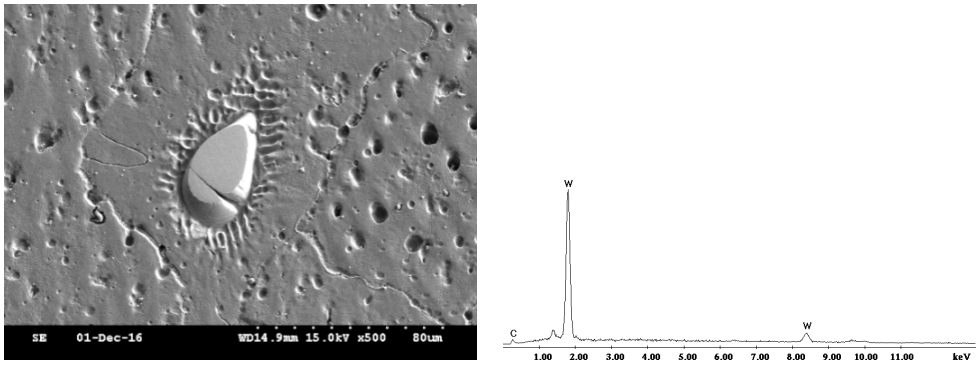

(A) (B)

Fig. 23. Morphology and energy spectrum of WC precipitates

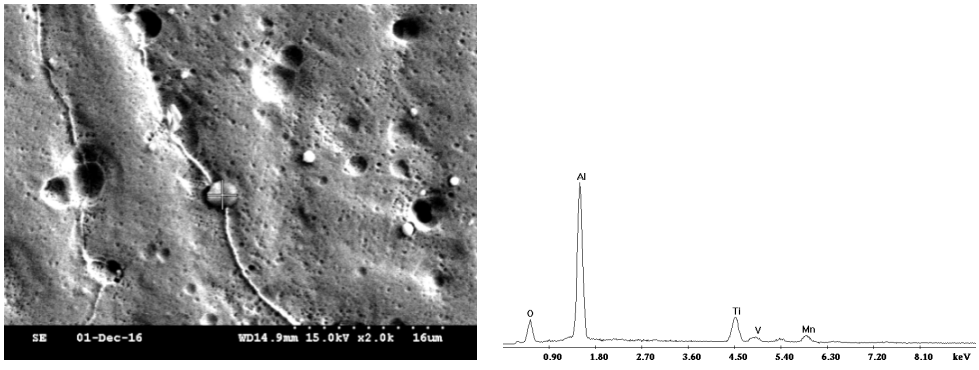

(A) (B)

Fig. 24. Precipitation of Al and Ti oxides

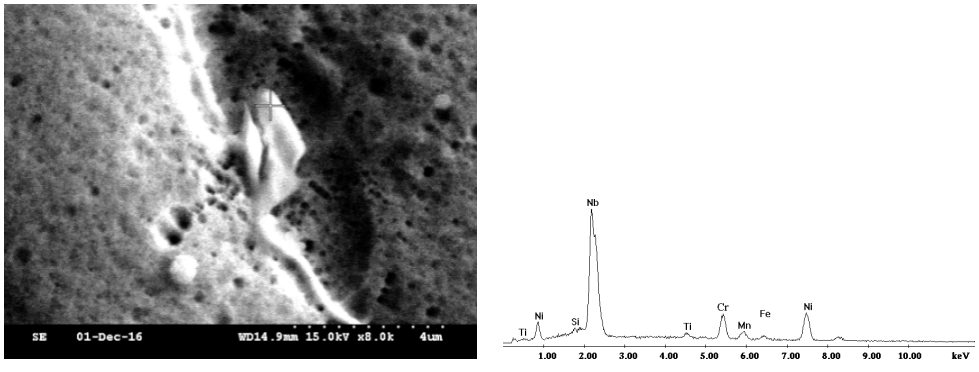

(A) (B)

Fig. 25. Precipitation of Nb carbide

Nb carbide are, respectively, about 1–2 μm and 3 μm, and it is distributed in the grain boundary discontinuously.

Figures 26–28 show the SEM and energy spectrum of the grain boundaries in the 1#, 2#, and 3# deposited metals, respectively. The compositions of these three deposited metal precipitates are shown in Tables 7–9, respectively. The average size of the precipitated phases is 0.98 μm, 1.21 μm, and 1.53 μm, respectively. It can be seen from the diagrams that the precipitates of the three deposited metals are distributed continuously at grain bound-

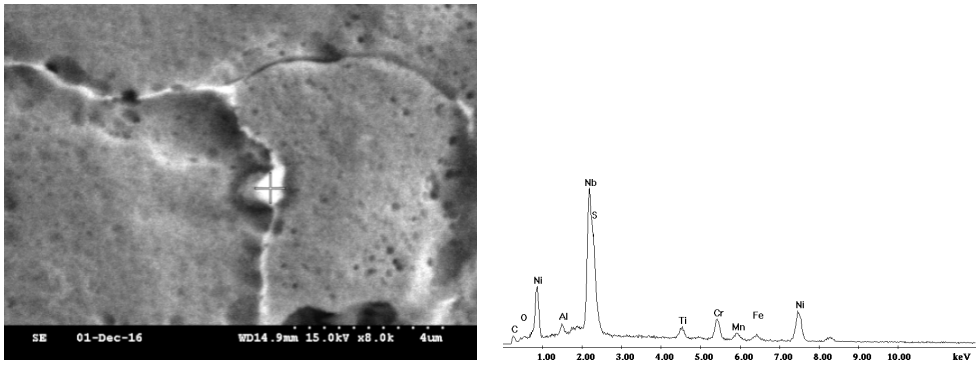

(A) (B)

Fig. 26. Morphology and energy spectrum of 1# deposited metal precipitates

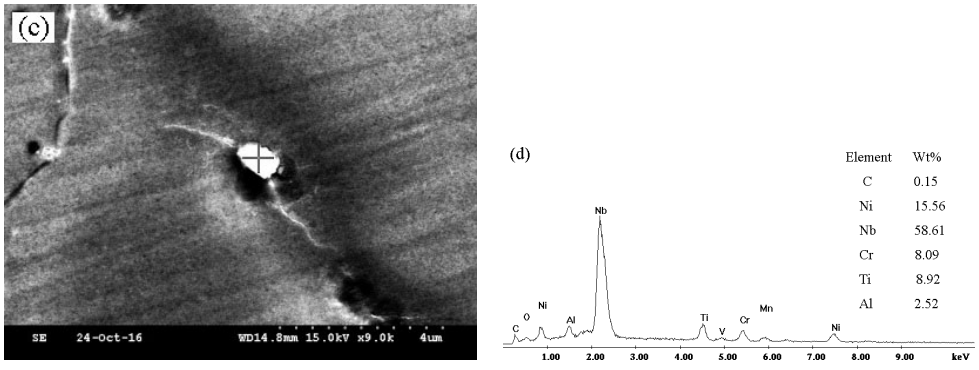

(A) (B)

Fig. 27. Morphology and energy spectrum of 2# deposited metal precipitates

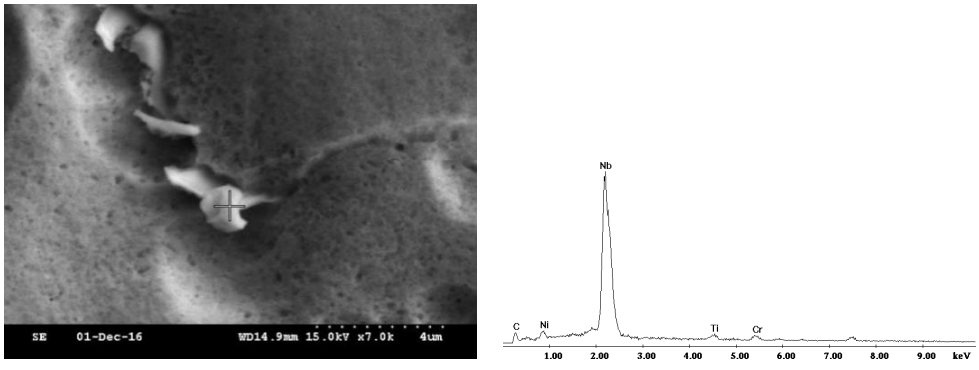

(A) (B)

Fig. 28. Morphology and energy spectrum of 3# deposited metal precipitates

aries, and the main precipitates are precipitated in the form of MC carbides. This is due to the high interdendritic energy, strong nucleation ability, and low solubility of Nb, Ti, and other elements in the austenite in the solidification process of the weld pool, since their compounds will form a segregation between dendrites, which helps to prevent grain boundary slipping and improves the performance of the deposited metal [22].

Table 7. Composition of 1# deposited metal precipitates (wt%)

NO.	Nb	Ni	Cr	Fe
1#	19.03	53.84	11.20	4.54

Table 8. Composition of 2# deposited metal precipitates (wt%)

NO.	Nb	Ni	Cr	Ti
2#	58.61	15.56	8.09	8.92

Table 9. Composition of 3# deposited metal precipitates (wt%)

NO.	Nb	Ni	Cr	Ti
3#	85.58	7.08	3.95	3.11

3.3.2.1. Effect of precipitates on initiation of crack initiation

The distribution and size of grain boundary precipitates have great influence on the strength and toughness of LNG under low temperature service environments. The precipitates along the grain boundary are nailed to the grain boundary, which makes grain boundary sliding difficult. In general, the continuous distribution of intergranular carbides is the path of crack initiation, and the solitary lumpy intergranular carbides are beneficial in preventing the initiation and propagation of cracks by reducing the slip and zigzag of the grain boundary. Therefore, there is no formation of wedge-shaped holes at the boundary of precipitates. If those grains are embellished with precipitates, grain boundary slippage will become difficult. The deformation is concentrated around the precipitates, which causes the formation of a circular hole. Since the crystallization crack is the process of stress at the later stage of solidification, the intergranular precipitates play the role of pinning grain boundaries, which also explains the favorable effect of Nb-containing carbides on the grain boundary. Therefore, the discontinuous grain boundary precipitates are favorable for strength and toughness. The more the carbides in the intergranular distribution, the more the medium size carbides are favorable to the growth resistance of the intergranular cracks, and the more obvious the pinning effect on the grain boundary.

There is a wedge crack at the junction of grain boundaries for 3# deposited metal, as shown in Figure 29. At the early stage of crack propagation, the precipitation of Nb carbide at the grain boundary shared the concentration region of the stress, which has caused a certain hindrance to crack initiation. The precipitates are mainly composed of Nb, and the precipitation of carbides hinders the growth of cracks. However, the precipitates are not distributed continuously on the whole grain boundaries, and thus the thermal cracking resistance of the weld metal is limited. At the same time, under the effect of the welding heat cycle, the low melting point eutectic impurity is near the grain boundary and redistributive to form the liquid film. When the tensile stress is drawn, the crack is produced along the grain boundary of the austenite [23].

The strength of the grain boundary is lower than that of the grain, and so when the external loading is applied, the grain boundary slip is faster, and there is a large strain concentration at the trigeminal boundary. If the strain concentration exceeds the local critical strain, micro cracks will form. The junction between precipitates and grain boundaries will produce strain concentration, thus sharing part of strain and reducing strain concentration at the trigeminal boundary. There are NbC precipitates at the grain boundaries, which share part of the strain load, and also pose some impediment to grain boundary slippage. The strain is distributed not only to the precipitates but also to the strain concentration at the bent grain boundaries. The total strain is shared at various locations.

Because of the particularity of its service environment, the pressure and temperature of LNG storage tanks vary with the changing amount of stored LNG. Two cases characterize the fracture of LNG storage tank. The first case is that the LNG storage tank does not contain any cracking; and the change of microstructure causes the damage of mechanical properties, such as toughness and so on, in the environment of constantly changing pressure and temperature. The second case is that there are cracks or other similar formations in LNG tanks, and the fracture is caused by the expansion of the main cracking. The fracture model is a grain boundary sliding and stress concentration model.

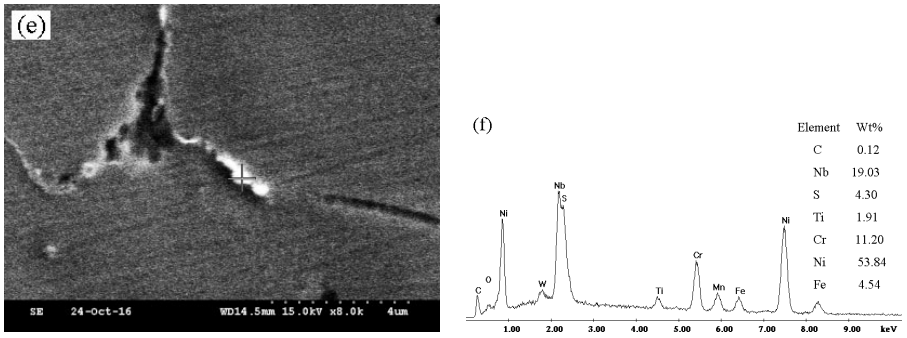

(A) (B)

Fig. 29. Morphology and EDS analysis of precipitates of deposited metal. **(A)** 3#SEM, **(B)** 3#EDS. EDS, energy dispersive spectrometer; SEM, scanning electron microscopy

Due to the change of temperature and pressure, the change of load leads to the maximum stress in the grain boundary in the direction of the maximum shear stress, and the stress is especially concentrated on the boundary of the three grains. If the stress cannot be relaxed by the plastic deformation of the grain in front of the interface or the movement of the grain boundary, then the stress concentration reaches the bonding strength at the grain boundary, and a crack will occur at the interface of the three grains, thus forming the wedge hole.

The intergranular precipitates in Ni-Cr-Mo series alloys are roughly classified into two groups according to the temperature range formed. The first type is precipitates with melting points higher than those of alloys, such as oxides of Al and Ti, which are larger in size and do not undergo remelting. The second kind of precipitates occur in the late solidification stage, such as eutectic MC carbides (M can be Nb or Ti). Their size is about 1–3 m, and they can pin solidified grain boundaries effectively, hinder grain growth, and facilitate the independent transformation of solidified grain boundaries into straight migrating grain boundaries, thus resulting in distorted grain boundary morphology. According to grain boundary slip theory, the boundary can effectively suppress crack propagation.

3.3.2.2. Role of precipitates in preventing crack propagation

The intergranular cracks and precipitates are shown in Figure 30. MC carbides pin grain boundaries and form zigzag grain boundaries, which hinder the growth of crystal cracks. Under the condition of an LNG tank serving at low temperature, the long straight austenite grain boundary is apt to slip when the liquid inside LNG is subject to an external force load, especially at the junction of the grain boundary, where the stress and strain are concentrated. When the strain exceeds the critical strain at the junction, a micro crack will appear, as shown in Figure 30.

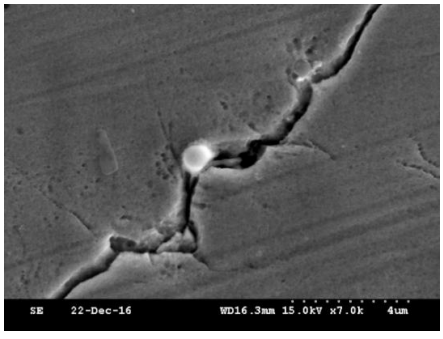

Fig. 30. Zigzag grain boundary

If there is precipitate on the austenite grain boundary, it will, on the one hand, bear part of the stress at the grain boundary where the precipitate is located, and play a certain role in sharing the stress at the junction of the grain boundary. On the other hand, MC carbides precipitated at grain boundaries play the role of zigzag grain boundaries in pinning grain boundaries, further sharing the stress, and thus increasing the stress bearing limit of intergranular crack initiation.

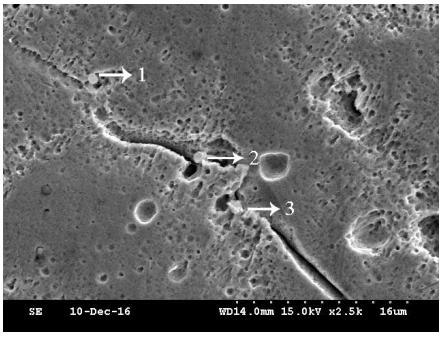

(A)

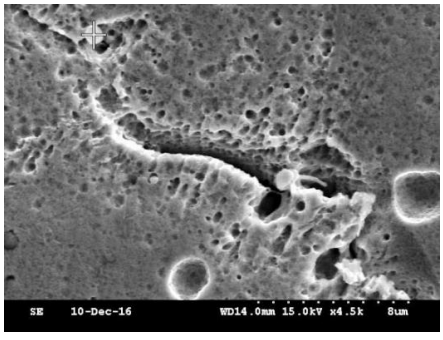

(B)

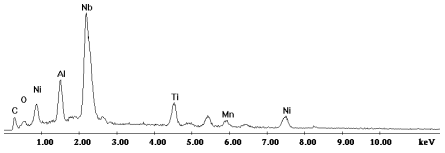

(C)

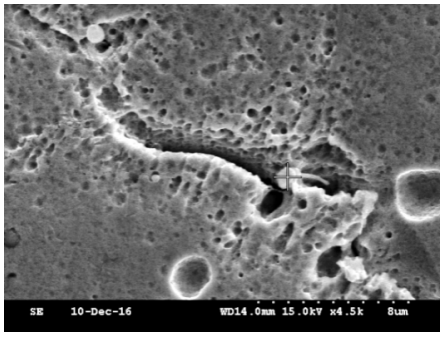

(D)

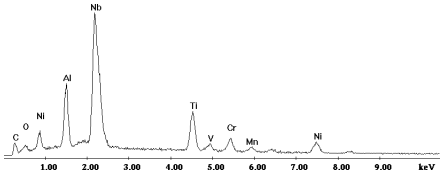

(E)

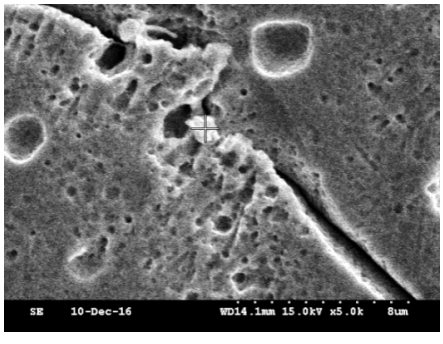

(F)

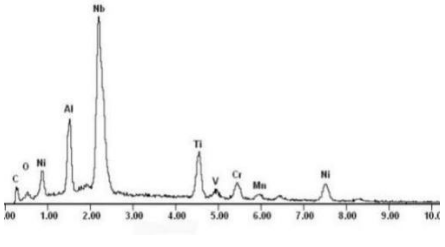

(G)

Fig. 31. Intergranular cracking and precipitates of the three deposited metals: **(A)** SEM, **(B)** First measuring point and element analysis, **(C)** Second measuring point and element analysis, **(D)** Third measuring point and element analysis. SEM, scanning electron microscopy

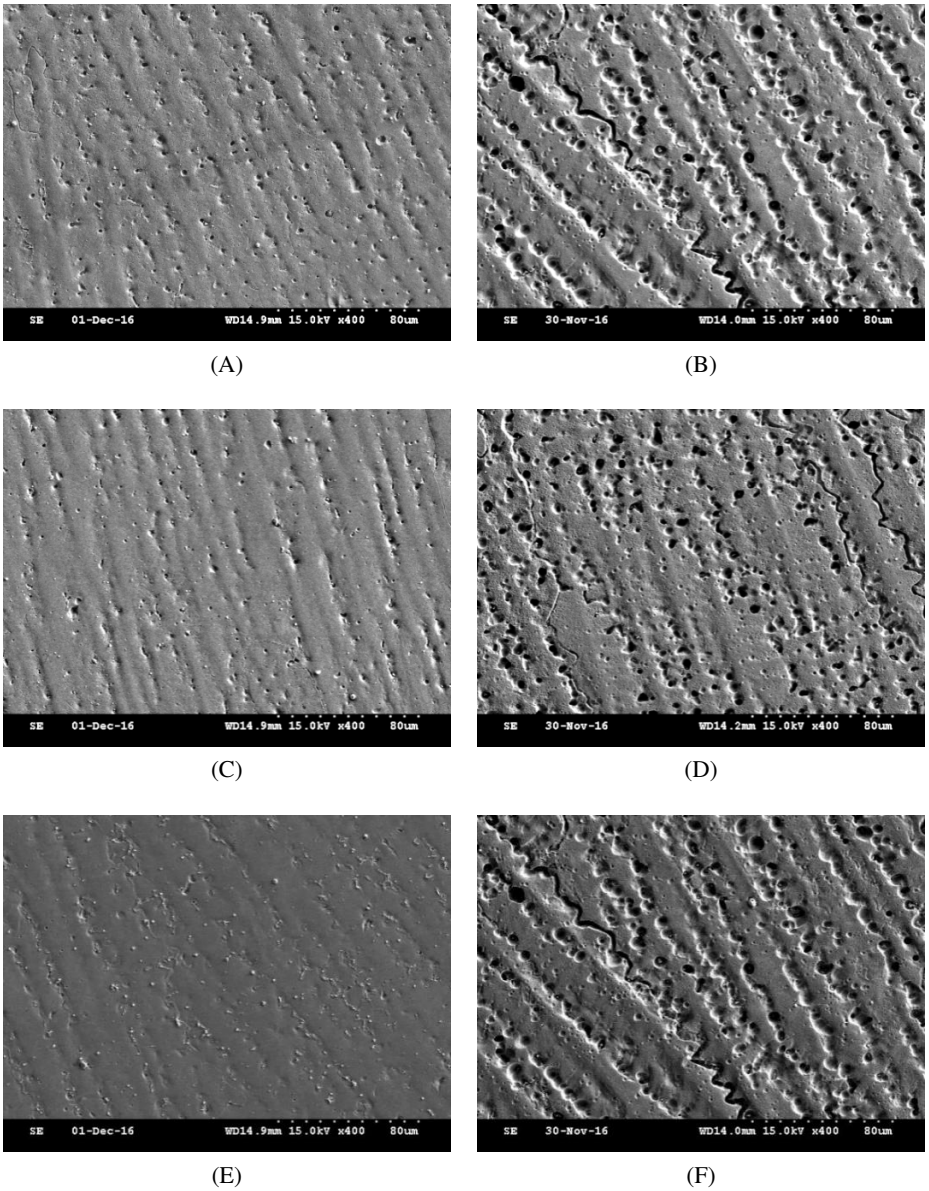

(A) (B)

(C) (D)

(E) (F)

Fig. 32. Precipitate morphologies: **(A, C, E)** root of 1#, 2#, 3# welding; **(B, D, F)** surface of 1#, 2#, 3# welding

Figure 31 shows the intergranular cracks with three precipitates distributed at the crack, and the composition of deposited metal precipitates is shown in Table 10. The energy spectrum reveals that these precipitates are mainly Nb carbides, together with a small amount of Al oxides. These precipitates pin the grain boundaries and make the straight grain boundaries become tortuous at the precipitates, which hinders the crack propagation along the grain boundaries.

Table 10. Composition of deposited metal precipitates (wt%)

Precipitate	**Nb**	**Ni**	**Al**	**Ti**
1	33.19	15.82	14.27	19.71
2	47.19	14.99	9.47	15.29
3	46.16	18.98	8.80	13.53

Generally speaking, the existence of intercrystalline precipitates leads to pinning and zigzag

Table 11. Tensile properties of welding rod deposited metal

No.	Tensile Strength (R_m) MPa	Yield strength ($R_{p0.2}$) MPa	Elongation (A)%	Section shrinkage (Z)%
1#	687	429	33.1	33
2#	705	478	32.5	34
3#	710	482	27.5	30

of grain boundaries and hinders the propagation of cracks, thus enhancing the low temperature strength and impact toughness of the materials.

Figure 32 shows the morphology of precipitates. The number of precipitates was analyzed using image-Pro-Plus software and 10 fields of view were randomly selected by SEM at the same multiple.

As shown in Figure 33, with the increase of Nb content, the amount of precipitates on roots and surfaces increased. In the three groups of deposited metal, the amount of precipitates on the surface is more than that on the root, which is because the root of the deposited metal is more diluted and the alloy content is slightly reduced, thus resulting in a relatively small amount of precipitates.

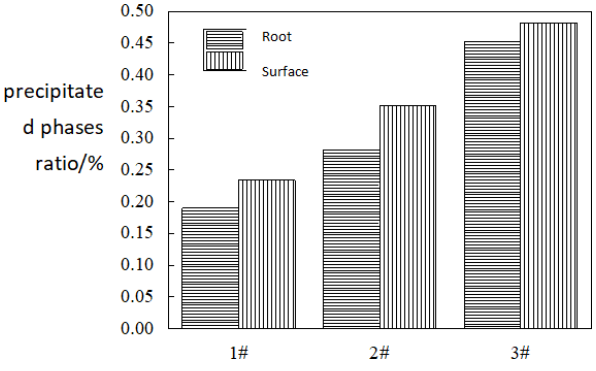

Fig. 33. Quantity of precipitated phases of the three deposited metals

3.4. Mechanical properties of deposited metal

3.4.1. Strength of deposited metal

Tensile properties of the No. 1 and No. 2 welding rod deposited metals are shown in Table 11. It can be seen that the deposited metals No. 1 and No. 2 possess sufficient tensile strength, which is attributed to the solid solution strengthening of Cr, W, Mo, Nb, and other elements in the deposited metals, so that the alloy has higher intragranular strength. At the same time, the carbide precipitated from the grain boundary enhances the grain boundary strength [24] and improves the strength of the deposited metal. Therefore, the solution strengthening and precipitation strengthening of No. 2 deposited metal with higher alloy element content are more significant, and the strength of the deposited metal is higher. The tensile strength and elongation of the deposited metal of No. 3 welding material are not up to the requirements of LNG equipment. The main reason is that the content of S is too high, and there are many intergranular cracks, as can be seen in Figure 34. This kind of crack significantly reduces the strength of the deposited metal, and so the content of S must be strictly controlled.

3.4.2. Hardness of deposited metal

Figure 35 shows the longitudinal hardness distribution of the deposited metal section. The average hardness values of the three deposited metals are 203.1 HV5, 211.6 HV5, and 212.2 HV5, respectively. It can be seen that with the increase of alloy content, the strengthening effect of the solid solution strengthening and precipitation phases is obvious, and the hardness of the deposited metals is improved in general. The hardness values of the three deposited metals decreased with moving toward the weld surface, but increased in different degrees near the deposited metal surface. Combined with the thermal cycle analysis of weld bead, it is considered that the hardness of austenite decreases gradually because the austenite grains in the root are more compact, and the precipitates decrease with the alloy composition dilution from the root to the surface.However, in the vicinity of the deposited metal surface, a rapid cooling rate prevails, and thus weld passes are not subject to the

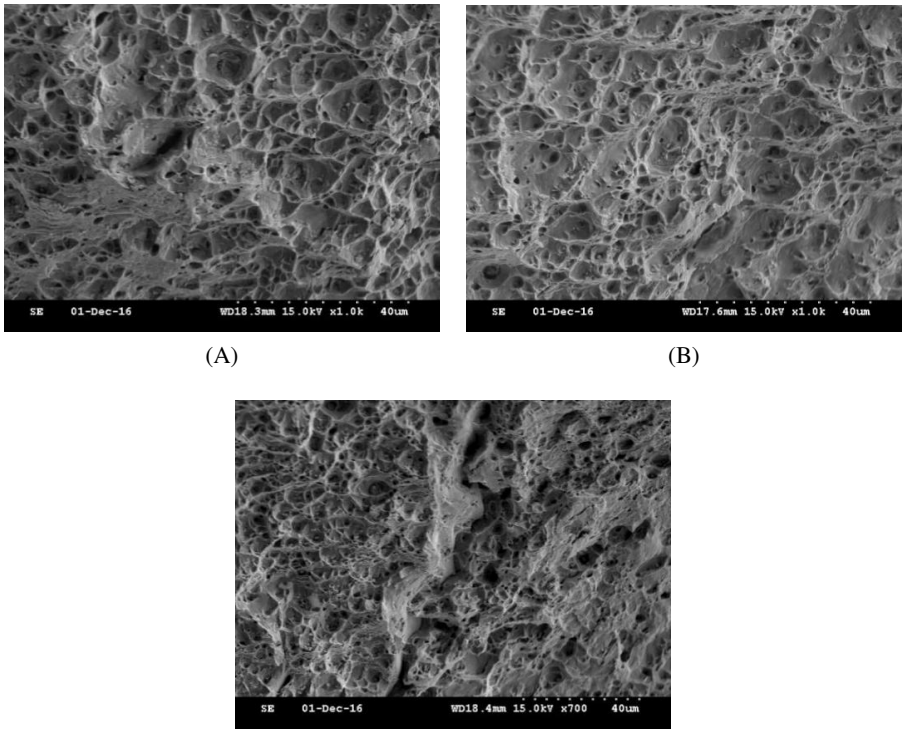

(A) (B)

(C)

Fig. 34. Intergranular crack in tensile test: **(A)** 1#; **(B)** 2#; **(C)** 3#

heat treatment effect. Therefore, the microstructure near the deposited metal surface is mainly austenite cellular crystal, and the grain is fine and uniform. Thus, the hardness of the alloy near the surface increases to a certain extent, and this is attributable to the fact that the alloy content is higher and the amount of precipitated phase increases.

3.4.3. Toughness of deposited metal

The impact toughness of the three deposited metals is shown in Table 12, and the test temperature is −196°C. According to the BS7777 standard, the impact energy of the weld is no less than 35 J, which shows that the impact test results meet the requirements. As can be seen from Table 12, the impact toughness from high to low is No. 1, No. 2, and No. 3, and the average impact values of No. 1 and No. 2 are much higher than that of No. 3. The main reasons are as follows: When the content of Ni exceeds 66%, the slip between austenite FCC lattices changes little with temperature, and there is no obvious transition from plastic to brittle state, and thus the toughness is better at low temperature. When conditions of low melting point are prevalent, the high S content in deposited metal No. 3 results in the formation of eutectic at the grain boundary, which increases the cracking tendency and leads to low temperature toughness.

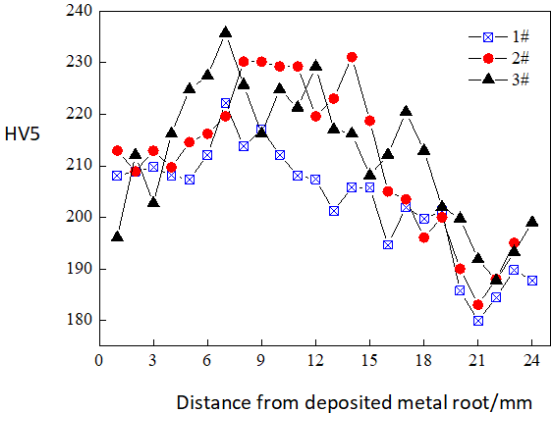

Fig. 35. Longitudinal distribution of hardness of deposited metal

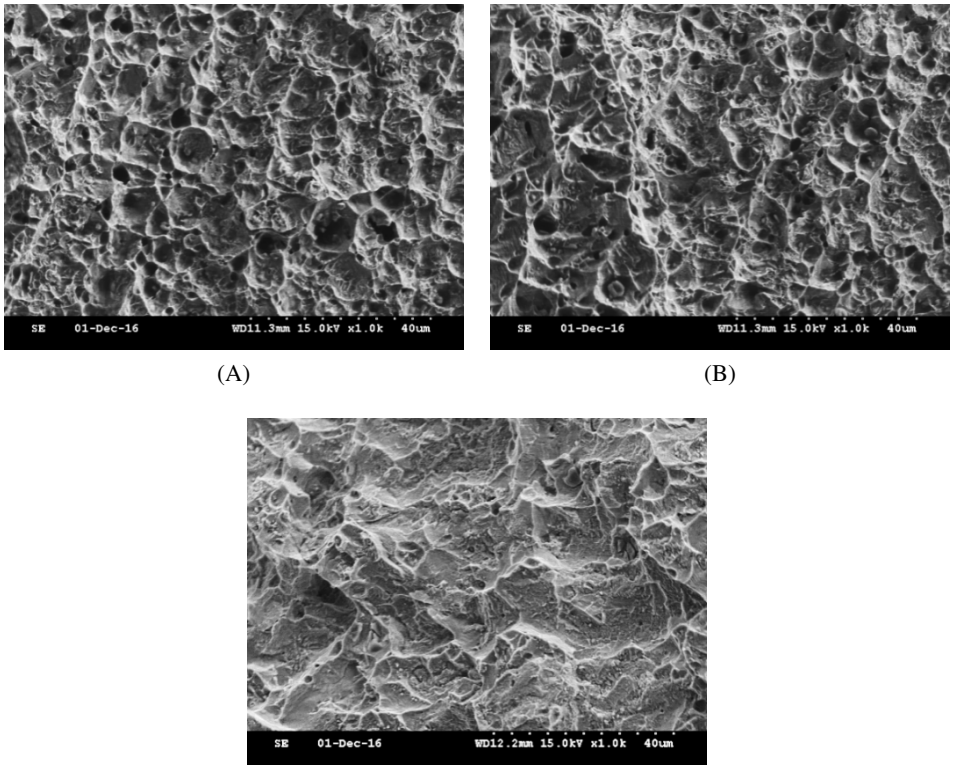

(A) (B)

(C)

Fig. 36. SEM morphologies of impact fracture of deposited metal: **(A)** 1#, **(B)** 2#, **(C)** 3#. SEM, scanning electron microscopy

Table 12. Impact resistance of deposited metal

No.	Akv/J
1	132, 133, 126, 140, 126
2	115, 123, 119, 112, 113
3	80, 89, 82, 95, 92

Figure 36 presents the SEM morphology of impact fracture of the three deposited metals. From Figure 36A, it can be seen that the dimple size of No. 1 deposited metal fracture is large and deep, there is a large-sized tearing edge, and the fracture surface fluctuates greatly, and thus the crack propagation consumes more energy and corresponds to higher impact toughness. Figure 36B shows the impact fracture morphology of deposited metal No. 2. The dimple depth is relatively shallow, the tearing edge undulation becomes smaller, and the crack propagation resistance is slightly reduced. Figure 36C shows the fracture morphology of deposited metal No. 3. The dimple size is small and the depth is shallow, the surface of the whole fracture is flat, and the dimple distribution assumes a parallel strip shape. It shows that the crack propagation direction is consistent, the crack propagation speed is fast after initiation, the energy consumption is low at fracture, and the final macroscopic performance is low impact absorption energy.

4. Conclusions

1. Nickel is beneficial to the stabilization of austenite matrix, and Mo, Cr, and W are used to improve the binding force between atoms. Strong carbide elements such as Nb, Ti, and V are added to form stable precipitates.
2. The existence of intercrystalline precipitates leads to pinning and zigzag of grain bound-

aries and hinders the propagation of cracks, thus enhancing the low temperature strength and impact toughness of the materials.

3. The newly developed No. 1 and No. 2 ENiCrMo-6 electrodes meet the requirements of LNG equipment. On the whole, No. 1 electrode has the best performance. The tensile strength of the deposited metal reaches 687 MPa, and the average impact energy at -196°C is 131 J.
4. Under low melting point conditions, it is easy for the S element in the welding rod to form eutectic with Ni and other elements and induce intergranular crack, and thus S content must be strictly controlled.
5. The mainly observed characteristics of the microstructure of weld metal are the presence of austenite and that of a large amount of carbide precipitation. The stress concentration at the junction of grain boundaries can easily cause cracks. MC carbide can retard the crack propagation. With the increase of Nb and other alloys, the strength and hardness increase gradually, but the plasticity and toughness are damaged to a certain extent.

References

[1] Jena PK, Mishra B, RameshBabu M, Babu A, Singh AK, SivaKumar K, et al. Effect of heat treatment on mechanical and ballistic properties of a high strength armour steel. Int J Impact Eng. 2010;37(3):242–9.

[2] Saha A, Mondal DK, Maity J. Effect of cyclic heat treatment on microstructure and mechanical properties of 0.6 wt% carbon steel. Mater Sci Eng A. 2010;527(16–17):4001–7.

[3] Hwang B, Lee CG. Influence of thermomechanical processing and heat treatments on tensile and Charpy impact properties of B and Cu bearing high-strength low-alloy steels. Mater Sci Eng A. 2010;527(16–17):4341–6.

[4] Aghajani A, Somsen C, Pesicka J, Bendick W, Hahn B, Eggeler G. Microstructural evolution in T24, a modified 2(1/4)Cr–1Mo steel during creep after different heat treatment. Mater Sci Eng A. 2009;510(10):130–5.

[5] Gao M, Zeng X, Hu Q, Yan J. Laser-TIG hybrid welding of ultra-fine grained steel. J Mater Process Technol. 2009;209(2):785–91.

[6] Wu Z, Jiang Q. Discussion on automatic submerged arc welding of 9%Ni steel in LNG storage tank. Installation. 2006;26(1):42–5.

[7] Du WS, Cao R, Yan YJ, Tian ZL, Peng Y, Chen JH. Fracture behavior of 9% nickel high-strength steel at various temperatures Part I. Tensile tests. Mater Sci Eng. 2008;86(4):611–25.

[8] Shin HS, Lee HM, Kim MS. Impact tensile behavior of 9% nickel steel at low temperature. Int J Impact Eng. 2000;24(6):571–81.

[9] Changhua Y. Research on weldability and welding technology of 9%Ni steel for LNG storage tank construction. Tianjin University; 2008.

[10] El-Batahgy AM, Gumenyuk A, Gook S, Rethmeier M. Comparison between GTA and laser beam welding of 9%Ni steel for critical cryogenic applications. J Mater Process Technol. 2018;261:193–201.

[11] Mu W, Li Y, Cai Y, Wang M. Cryogenic fracture toughness of 9%Ni steel flux cored arc welds. J Mater Process Technol. 2018;252:804–12.

[12] Li Y, Yang F. Research and application of 9Ni steel and its welding materials. Welded Pipe Tube. 2015;11:37–40.

[13] Liu H, Wang D, Wei H, Zhang Y, Li J, Zhao A. Commercial development of high performance Ni based corrosion resistant alloys. Metal Funct Mater. 2011;7:10–6.

[14] Yuan L, Hu R, Gao X, Li Z. Generation of high-performance Ni-Cr-Mo-based superalloys via γ to DO22 superlattice ordered phase transformation upon addition of trace alloying elements. Mater Sci Eng A. 2018;738(9):38–43.

[15] Kamali-Heidari E, Xu ZL, Sohi MH, Ataie A, Kimb JK. Core-shell structured Ni3S2 nanorods grown on interconnected Ni-graphene foam for symmetric supercapacitors. Electrochim Acta. 2018;271(1):507–18.

[16] Wang ZQ, Wang XL, Nan YR, Shang CJ, Wang XM, Liu K, et al. Effect of Ni content on the microstructure and mechanical properties of weld metal with both-side submerged arc welding technique. Mater Charact. 2018;138(4):67–77.

[17] Gioielli PC, Zettlemoyer N. SN fatigue tests of 9% nickel steel weldments. Lisbon: Proceedings of the Sixteenth (2007) International Offshore and Polar Engineering Conference; 2007: 3318.

[18] Hilkes J, Neessen F, Caballero S. Electrodes for welding 9% nickel steel. Weld J. 2004;83(1):30–7.

[19] Suo J, Feng D, Suo H, Cui W. Study on the dissolution mechanism of WC particles during surfacing process. Funct Mater. 2003;34(2):221–3.

[20] Lindemer TB, Besmann TM, Johnson CE. Thermodynamic review and calculations—alkali-metal oxide systems with nuclear fuels, fission products, and structural materials. J Nucl Mater. 1981;100(1–3):178–226.

[21] Guan XR, Zheng Z, Liu EZ, Zhai YC. Effect of Ti on solidification segregation of DZ68 alloy. J Northeast Univ (NATURAL SCIENCE). 2010;31(2):214–6.

[22] Bagheri Y, Kamali H, Kamali E, Nedjad SH. Formation of nodular bainite in an Fe-9.10Ni-0.06C (wt.%) alloy: a new microstructure for cryogenic steels. Scripta Mater. 2022;208:14343.

[23] Kinney CC, Pytlewski KR, Khachaturyan AG, Morris JW. The microstructure of lath martensite in quenched 9Ni steel. Acta Mater. 2014;69(5):372–85.

[24] Chen SH, Zhao MJ, Li XY, Rong LJ. Compression stability of reversed austenite in 9Ni steel. J Mater Sci Technol. 2012;28(6):558–61.

Received 2021-08-16
Accepted 2021-12-19